Supporting Information for "Modifying Surface Energy of Graphene via Plasma-based Chemical Functionalization to Tune Thermal and Electrical Transport at Metal Interfaces"

Brian M. Foley,[1]* Sandra C. Hernández,[2] John C. Duda,[1]
Jeremy T. Robinson,[3] Scott G. Walton,[2]* Patrick E. Hopkins[1]*

(1) Department of Mechanical and Aerospace Engineering
University of Virginia, Charlottesville, Virginia 22904, USA

(2) Plasma Physics Division
Naval Research Laboratory, Washington, DC 20375, USA

(3) Electronics Science & Technology Division
Naval Research Laboratory, Washington, DC 20375, USA

E-mail: bmf4su@virginia.edu, scott.walton@nrl.navy.mil, peh4v@virginia.edu

June 29, 2015

Growth and Transfer of Single-layer Graphene Samples

Growth: Graphene was grown via low-pressure chemical vapor deposition (CVD) in Cu foil "enclosures" [1, 2] at a temperature of 1030°C. The growth system has a base pressure of 2 mtorr and during growth, both hydrogen and methane gases were introduced to a total pressure between 30-100 mtorr (H_2:CH_4, 1:10). After one hour the copper substrates were removed from the hot zone of the furnace and quenched under flowing H_2/CH_4 at a total pressure of 30 mtorr.

Transfer: We use the conventional wet-chemical approach to transfer graphene to SiO_2/Si surfaces. A PMMA support layer is deposited on the graphene/Cu substrate to mechanically support the graphene film while the underlying copper substrate is etched away. Afterwards, the PMMA/graphene film is rinsed in a water bath and transferred to a target substrate, the PMMA is removed with acetone, and then the samples are annealed in high vacuum (10E-6 to 10E-7 torr) at 250°C. Vacuum annealing has been shown to be an effective method for the reduction of PMMA residue from transferred CVD graphene, leaving only trace amounts of decomposed PMMA [3, 4]. Subsequent to film transfer, we use shadow masking for plasma functionalization and metallization to avoid photolithography and thereby further reduce extrinsic sources of carbonaceous residues.

Ex-situ X-ray Photoelectron Spectroscopy (XPS) Measurements and Data Analysis

Following plasma functionalization, ex-situ X-ray Photoelectron Spectroscopy (XPS) measurements using a monochromatic X-ray photoelectron spectrometer (K-Alpha XPS System). Measurements were acquired with a 400 micro-meter spot size, with a pass energy of 20 eV, dwell time of 50 ms, and 20 scans per high resolution spectra. Surface composition was determined by fitting the high resolution elemental spectra using commercially available Unifit software. The percentages of functional groups was determined by using the XPS high-resolution spectra. The actual calculation was performed by de-convolution of the high resolution C1s spectra using commercially available Unifit software package. Subcomponents of the C1s region were identified by first fitting the lowest binding energy component (sp^2 C-C) and restricting the full-width-half-maximum of that component to all other sub-components. Subcomponents were assigned by their binding energy location and relative distance to the lowest binding energy component. The contribution of the individual functional groups was determined by their respective sub-component percent contribution of the total area of the C1s. In some instances, tracking of the C1s oxygen functionalities is challenging since C-OH, C-O and sp^3 carbon have overlapping binding energies. These XPS measurements were performed on witness un-patterned samples that were functionalized simultaneously with other samples.

Time Domain Thermoreflectance (TDTR)

Experimental Setup: TDTR is a non-contact, optical pump-probe technique utilizing ultra-fast sub-picosecond (sub-ps) laser pulses to interrogate the progression of a thermal wave from a top layer through the layers beneath it. [5] An exponentially-decaying curve of the change in temperature at the surface of the sample (the gold film) as a function of time is generated by delaying the arrival of the probe pulse (the temperature sensor) relative to the pump pulse (the heating event). By fitting this curve to a multi-layer model, values for various parameters of interest, including the thermal conductivities of materials or the thermal boundary conductance between two dissimilar materials, can be extracted. Thorough descriptions of both the experiment and the model can be found in Refs. [5–9]. For our experiment, we use an 80 MHz rep-rate Ti:Sapphire oscillator producing sub-ps pulses at a wavelength of 800 nm. We split the output from the oscillator to create our pump and probe beams. The pump beam is modulated by a linearly-amplified 11.39 MHz sinusoid and then converted to 400 nm wavelength light using a BIBO crystal, while the probe beam is sent down a mechanical delay stage to delay the arrival of the probe relative to the pump at the sample surface. A photodiode and lock-in amplifier (SRS 844) is used to monitor the ratio of the in-phase and out-of-phase signals from the reflected probe beam at the modulation frequency of the pump.

Data Analysis: The thermoreflectance signals acquired using TDTR were fit to a two layer model (90 nm Au on semi-infinite SiO_2) to extract the thermal boundary conductance between the Au and SiO_2. The decision to treat the SiO_2 layer as semi-infinite is valid due to the extremely shallow thermal penetration depth of the thermal wave in this case. Due to the low thermal conductivity of the SiO_2 ($\kappa_{SiO_2} = 1.28\,\mathrm{W\,m^{-1}\,K^{-1}}$) and the 11.39 MHz modulation frequency of the pump beam, the thermal penetration depth (δ) in this particular instance is approximately 150 nm. As a result, the thermal wave induced by the modulated pump beam will only propagate about half way into the 300 nm layer of SiO_2 and the modulated TDTR response will not be sensitive to the Si substrate, nor to the interface conductance between the SiO_2 and Si. Three TDTR scans were performed on each sample in the study to account for measurement uncertainty, and an additional

uncertainly of $\pm$ 3 nm in the thickness of the 90 nm Au transducer layer was included when fitting the TDTR data to the multilayer thermal model.

When fitting the data to the model, the SiO_2 was fixed at its literature value and the only free parameter was the Au/SiO_2 thermal boundary conductance, which includes the graphene monolayer. However, any contribution from the atomically-thin graphene sheet is assumed negligible, which has been confirmed in several previous works. [10, 11] The value extracted from the fit is actually an effective conductance which is a sum of the contributions from the interfaces on either side of the graphene.

$$h_{\mathrm{K,metal/SLG/SiO_2}} = \left(h^{-1}_{\mathrm{K,metal/SLG}} + h^{-1}_{\mathrm{K,SLG/SiO_2}} \right)^{-1} \tag{1}$$

From the measured total conductance and the literature value for the thermal boundary conductance at an SLG/SiO_2 interface ($\approx$ 85 MW m^{-2} K^{-1}), [12] equation (1) can be used to determine the conductance across the functionalized Au/SLG interfaces. These results are provided in Figure 3 and Table 1 in the main manuscript.

Transfer Length Method (TLM)

Experimental Methods: Transfer length method (TLM) [13–15] structures were fabricated to interrogate the electrical contact resistance. In this study the TLM structures consisted of a series of identically sized contact pads with different spacings ranging from $\approx$ 50 to 150 μm between each adjacent pad in order to extrapolate the contact resistance between the pad and the material underneath. Figure 1(e) in the main manuscript is an optical image of the TLM geometry used in this study, including the measured distances between pads. By measuring the total resistance between two adjacent pads and plotting these resistances as a function of the spacing between the pads, the resistance due to the contact interface alone can be determined. In the limit that the spacing between pads goes to zero, the device resistance is simply that of the two contacts alone. Therefore, the metal/SLG contact resistance (R_{C}) can be obtained by taking half of the y-intercept of the linear fit to the TLM data. Furthermore, the width-normalized contact resistivity (ρ_{C}) can be obtained by multiplying R_{C} by the width of the contact pads. Measurements of the pad-to-pad resistances in the TLM patterns were performed on a probe station (JmicroTechnology, LMS-2709) using kelvin-style, dual-tip probes (Cascade MicroTech, DCP-150K-25) connected via triax cabling to a SourceMeter unit (SMU, Keithley Instruments 2612A). The kelvin-style probes enable a local measurement of the potential at the pad while under constant current bias (1 mA), thereby eliminating the resistances due to the cabling and providing a measurement of the pad-to-pad resistance alone. Ten TLM patterns were measured for each sample in the study and the ten resistances measured at identical separation distances were averaged together.

Data Analysis: Figure 1 shows the TLM data collected from the samples in the study and Table 2 from the main manuscript should be referenced for the ensuring discussion. Linear fits were applied to the data to extract the contact resistance (R_{C}) and the sheet resistivity (R_{S}) of the graphene between the contacts, and the width-normalized contact resistivity (ρ_{C}) was calculated by multiplying R_{C} by the approximate width of the contact (450 μm). Plots (a) and (b) in Fig. 1 are the Au/SLG and Au/Ti/SLG contacts, respectively, and we notice that both ρ_{C} and R_{S} are quite similar

between the two contact types.

Plots (c) and (d) show the TLM data for contacts that were functionalized with ≈ 5 at $\%$ oxygen and fluorine, respectively. As with the Au/SLG and Au/Ti/SLG data, a linear fit was applied to the data to extract ρ_{C} and R_{S}, and we immediately notice a difference between the contacts functionalized with the different species. While the oxygen functionalized contacts show little to no change in ρ_{C}, the fluorine functionalized contacts exhibit a three to four-fold increase in ρ_{C} over that of a Au/SLG of Au/Ti/SLG contact. Additionally, the fits to the data in (c) and (d) show that the R_{S} of the graphene in the channel has increased compared to the non-functionalized samples in (a) and (b). We attribute this to the presence of functional groups in the channel along the contact edge, as the use of the physical mask during plasma functionalization will likely not produce sharp edges. [16, 17] These adsorbates will affect the local band-structure and density of states of the graphene, resulting in the increased sheet resistance.

Plots (e) and (f) in Fig. 1 highlight the unique behavior at coverages of ≥ 10 at $\%$ oxygen or fluorine. In both sets of data, there is a departure from the linear trends observed in plots (a) through (d). In the oxygen functionalized cases, the device resistances as a function of contact separation saturate for distances greater than 75-100 μm. By comparison, saturation occurs for contact separations greater than 100-125 μm in the case of fluorine functionalization. For contact separations less than these saturation points, the device resistances decrease and exhibit the linear trend that is expected from these TLM measurements.

This non-linearity in the TLM measurements is due to spatial variations in the sheet resistance of the graphene. As noted earlier, these variations are attributed to the presence of functional groups in the channel along the contact edge. In previous works (Refs. [16, 17]), it was demonstrated that the spatial distribution of adsorbates deposited via plasma-functionalization on graphene can be controlled through a variety of factors, including the thickness of the mask and the height of the mask relative to the graphene underneath. In this work, the physical mask was used for both functionalization and the subsequent deposition of gold. It is very likely that this leads to a certain 'softness' in the edge profiles. More specifically, one expects a small gradient in the functional

group surface density, a mismatch between the gold and functional groups, and a slope in the metal contact edge wall. These effects are likely to become more pronounced with increasing coverage as the amount in the channel increases, affecting both the local carrier density and band-structure of the graphene in these regions, ultimately affecting the electronic transport properties in these regions. [18–21]

The inflection points in Figs. 1(e) and (f) indicate a characteristic length of influence over which functional groups emanating from the contact edges into the graphene channels impact the resistance. With oxygen adsorbates, the inflection point occurs at an approximate contact separation of 75 μm, while for fluorine adsorbates, the inflection occurs at around 100 μm. The reasons for this difference are unknown but might be related to how each moiety impacts carrier density and mobility or Au deposition. For contact separations greater than the observed inflection points, the saturation of the device resistances is likely due to the infinitesimal amount of resistance being added as a region of non-functionalized graphene increases between the contacts.

TLM analysis can be applied to the resistance data for contact separations less than the inflection points to extract R_{S} of the functionalized graphene in the channel, as well as ρ_{C} of the functionalized contacts. In the case of oxygenated graphene, both R_{S} and ρ_{C} increase by more than an order of magnitude with increasing percent coverage. For fluorinated samples, R_{S} increases by a factor of 2-4 compared to pristine graphene but shows no dependence on coverage. Interestingly, ρ_{C} actually decreases with increasing coverage, approaching values observed in the non-functionalized contact case (Au/SLG and Au/Ti/SLG). The increases in R_{S} can be attributed to a variety of effects caused by the presence of the adsorbates on the graphene in the channel, including distortion of the electronic band structure, doping, and an increase in carrier scattering sites. [18–21]

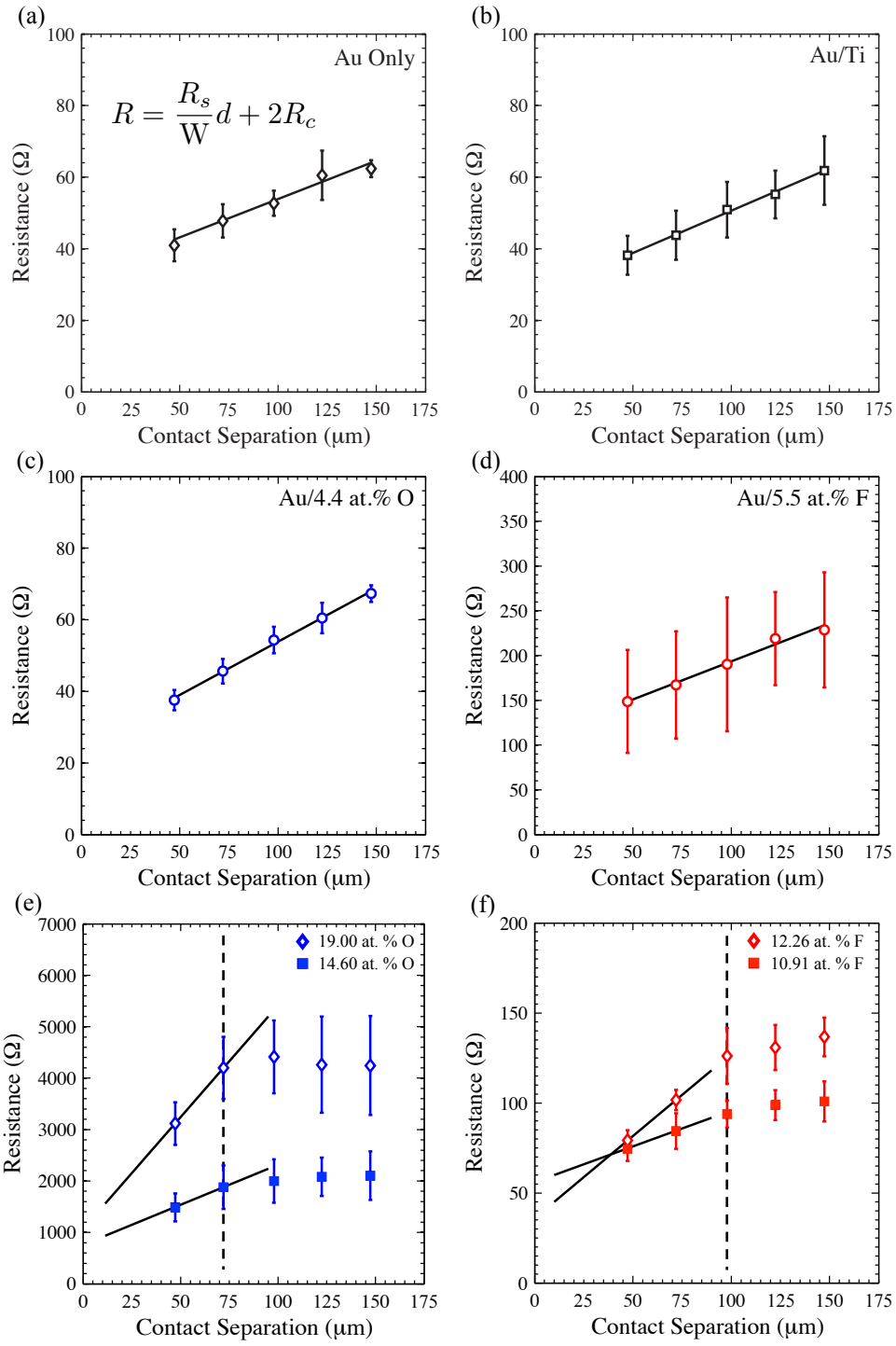

Figure 1: Transfer length method (TLM) data of the samples fabricated for the electrical part of the study. The data points and error bars represent the average values and standard deviations for measurements conducted on ten different TLM patterns per sample. Linear fits were applied to the data to extract R_{C}, ρ_{C} and the sheet resistivity (R_{S}) of the graphene between the contacts via TLM analysis.

References

[1] X. Li, W. Cai, J. An, S. Kim, J. Nah, D. Yang, R. Piner, A. Velamakanni, I. Jung, E. Tutuc, S. K. Banerjee, L. Colombo, and R. S. Ruoff, "Large-area synthesis of high-quality and uniform graphene films on copper foils," *Science*, vol. 324, no. 5932, pp. 1312–1314, 2009.

[2] X. Li, C. W. Magnuson, A. Venugopal, R. M. Tromp, J. B. Hannon, E. M. Vogel, L. Colombo, and R. S. Ruoff, "Large-area graphene single crystals grown by low-pressure chemical vapor deposition of methane on copper," *Journal of the American Chemical Society*, vol. 133, no. 9, pp. 2816–2819, 2011. PMID: 21309560.

[3] A. Pirkle, J. Chan, A. Venugopal, D. Hinojos, C. W. Magnuson, S. McDonnell, L. Colombo, E. M. Vogel, R. S. Ruoff, and R. M. Wallace, "The effect of chemical residues on the physical and electrical properties of chemical vapor deposited graphene transferred to silicon dioxide," *Applied Physics Letters*, vol. 99, no. 12, pp. –, 2011.

[4] Y.-C. Lin, C.-C. Lu, C.-H. Yeh, C. Jin, K. Suenaga, and P.-W. Chiu, "Graphene annealing: How clean can it be?," *Nano Letters*, vol. 12, no. 1, pp. 414–419, 2012.

[5] D. G. Cahill, K. Goodson, and A. Majumdar, "Thermometry and thermal transport in micro/nanoscale solid-state devices and structures," *J. Heat Transf.*, vol. 124, no. 2, pp. 223–241, 2002.

[6] D. G. Cahill, W. K. Ford, K. E. Goodson, G. D. Mahan, A. Majumdar, H. J. Maris, R. Merlin, and S. R. Phillpot, "Nanoscale thermal transport," *Journal of Applied Physics*, vol. 93, no. 2, pp. 793–818, 2003.

[7] D. G. Cahill, "Analysis of heat flow in layered structures for time-domain thermoreflectance," *Rev. Sci. Instrum.*, vol. 75, no. 12, pp. 5119–5122, 2004.

[8] A. J. Schmidt, X. Chen, and G. Chen, "Pulse accumulation, radial heat conduction, and

anisotropic thermal conductivity in pump-probe transient thermoreflectance," *Rev. Sci. Instrum.*, vol. 79, no. 11, p. 114902, 2008.

[9] P. E. Hopkins, L. M. Phinney, J. R. Serrano, and T. E. Beechem, "Effects of surface roughness and oxide layer on the thermal boundary conductance at aluminum/silicon interfaces," *Phys. Rev. B*, vol. 82, p. 085307, 2010.

[10] Y. K. Koh, M.-H. Bae, D. G. Cahill, and E. Pop, "Heat conduction across monolayer and few-layer graphenes," *Nano Letters*, vol. 10, no. 11, pp. 4363–4368, 2010.

[11] P. E. Hopkins, M. Baraket, E. V. Barnat, T. E. Beechem, S. P. Kearney, J. C. Duda, J. T. Robinson, and S. G. Walton, "Manipulating thermal conductance at metal–graphene contacts via chemical functionalization," *Nano Letters*, vol. 12, no. 2, pp. 590–595, 2012.

[12] Z. Chen, W. Jang, W. Bao, C. N. Lau, and C. Dames, "Thermal contact resistance between graphene and silicon dioxide," *Applied Physics Letters*, vol. 95, no. 16, p. 161910, 2009.

[13] F. Xia, V. Perebeinos, Y.-m. Lin, Y. Wu, and P. Avouris, "The origins and limits of metal-graphene junction resistance," *Nat Nano*, vol. 6, pp. 179–184, 03 2011.

[14] O. Balci and C. Kocabas, "Rapid thermal annealing of graphene-metal contact," *Applied Physics Letters*, vol. 101, no. 24, p. 243105, 2012.

[15] J. S. Moon, M. Antcliffe, H. C. Seo, D. Curtis, S. Lin, A. Schmitz, I. Milosavljevic, A. A. Kiselev, R. S. Ross, D. K. Gaskill, P. M. Campbell, R. C. Fitch, K.-M. Lee, and P. Asbeck, "Ultra-low resistance ohmic contacts in graphene field effect transistors," *Applied Physics Letters*, vol. 100, no. 20, p. 203512, 2012.

[16] S. C. Hernández, C. J. C. Bennett, C. E. Junkermeier, S. D. Tsoi, F. J. Bezares, R. Stine, J. T. Robinson, E. H. Lock, D. R. Boris, B. D. Pate, J. D. Caldwell, T. L. Reinecke, P. E. Sheehan, and S. G. Walton, "Chemical gradients on graphene to drive droplet motion," *ACS Nano*, vol. 7, no. 6, pp. 4746–4755, 2013.

[17] S. C. Hernández, F. J. Bezares, J. T. Robinson, J. D. Caldwell, and S. G. Walton, "Controlling the local chemical reactivity of graphene through spatial functionalization," *Carbon*, vol. 60, no. 0, pp. 84 – 93, 2013.

[18] N. Leconte, J. Moser, P. Ordejón, H. Tao, A. Lherbier, A. Bachtold, F. Alsina, C. M. Sotomayor Torres, J.-C. Charlier, and S. Roche, "Damaging graphene with ozone treatment: A chemically tunable metalinsulator transition," *ACS Nano*, vol. 4, no. 7, pp. 4033–4038, 2010.

[19] I. Childres, L. A. Jauregui, J. Tian, and Y. P. Chen, "Effect of oxygen plasma etching on graphene studied using raman spectroscopy and electronic transport measurements," *New Journal of Physics*, vol. 13, no. 2, p. 025008, 2011.

[20] C. Mathieu, B. Lalmi, T. O. Menteş, E. Pallecchi, A. Locatelli, S. Latil, R. Belkhou, and A. Ouerghi, "Effect of oxygen adsorption on the local properties of epitaxial graphene on sic (0001)," *Phys. Rev. B*, vol. 86, p. 035435, Jul 2012.

[21] J. T. Robinson, J. S. Burgess, C. E. Junkermeier, S. C. Badescu, T. L. Reinecke, F. K. Perkins, M. K. Zalalutdniov, J. W. Baldwin, J. C. Culbertson, P. E. Sheehan, and E. S. Snow, "Properties of fluorinated graphene films," *Nano Letters*, vol. 10, no. 8, pp. 3001–3005, 2010.